ARCHIVIO ISTITUZIONALE DELLA RICERCA

Alma Mater Studiorum Università di Bologna
Archivio istituzionale della ricerca

Inter-scale interaction in pipe flows at high Reynolds numbers

This is the final peer-reviewed author's accepted manuscript (postprint) of the following publication:

Published Version:
Zheng, X., Bellani, G., Mascotelli, L., Orlu, R., Ianiro, A., Vila, C.S., et al. (2022). Inter-scale interaction in pipe flows at high Reynolds numbers. EXPERIMENTAL THERMAL AND FLUID SCIENCE, 131, 1-12 [10.1016/j.expthermflusci.2021.110529].

Availability:
This version is available at: https://hdl.handle.net/11585/844627 since: 2024-09-05

Published:
DOI: http://doi.org/10.1016/j.expthermflusci.2021.110529

Terms of use:

Some rights reserved. The terms and conditions for the reuse of this version of the manuscript are specified in the publishing policy. For all terms of use and more information see the publisher's website.

This item was downloaded from IRIS Università di Bologna (https://cris.unibo.it/).
When citing, please refer to the published version.

(Article begins on next page)

07 October 2026

Inter-scale interaction in pipe flows at high Reynolds numbers

Xiaobo Zheng[a,b], Gabriele Bellani[c], Lucia Mascotelli[c], Ramis Örlü[c,d], Andrea Ianiro[e], Carlos Sanmiguel Vila[e], Stefano Discetti[e], Jacopo Serpieri[f], Marco Raiola[e], Alessandro Talamelli[c], Ye Li[a,b,g], Nan Jiang[h]

[a] *School of Naval Architecture, Ocean and Civil Engineering, Shanghai Jiao Tong University, Shanghai 200240, China*
[b] *Lab of Multiple Function Towing Tank, Shanghai Jiao Tong University, Shanghai 200240, China*
[c] *Dipartimento di Ingegneria Industriale, Università di Bologna, Forlì 47100, Italy*
[d] *Department of Engineering Mechanics, KTH Royal Institute of Technology, 10044 Stockholm, Sweden*
[e] *Aerospace Engineering Research Group, Universidad Carlos III de Madrid, 28911, Leganés, Spain*
[f] *Institute of Fluid Mechanics, Karlsruhe Institute of Technology, 76131, Karlsruhe, Germany*
[g] *State Key Lab of Ocean Engineering, Shanghai Jiao Tong University, Shanghai 200240, China*
[h] *School of Mechanical Engineering, Tianjin University, Tianjin 300354, China.*

Abstract

Hot-wire measurements of the streamwise velocity are conducted in the large-scale pipe-flow facility CICLoPE in the friction Reynolds number range of $7800 \leqslant Re_\tau < 40000$. Measurements are performed both with a rake of five synchronised probes arranged at different radial locations, and through a radial scan with a single wire traversing the whole pipe radius. Correlation-based analysis is used to extract features of inter-scale modulation in turbulent pipe flows. The Re_τ-independence of geometric features is shown with the outer scaling. Very-large-scale motions keep the vertical coherence to the wall through the whole pipe radius, while for the large-scale motions, the local coherence gradually become isotropic as the structure centre moves far away from the wall. From results obtained with the one-point amplitude modulation (AM) correlation function map, the AM effect is characterised by positive correlations observed in the inner region, while an opposite AM effect characterised by negative correlations is observed in the outer region. The strongest AM effect (with the maximum correlations) and the zero net-modulation (with zero correlations) show that the phase difference between large and small scales has a linear relation with the logarithm of the outer-scaled wall distance, but the strongest opposite effect (with the negative maximum correlations) behaves with the phase difference independent of the outer scaled wall-normal distance. Two-point AM coefficient maps, which give richer spatial information in the outer region than the one-point map, present the Re_τ-independence for AM and opposite effects within the present Re_τ range. In addition, the relative variation of the two effects in the coexisting wall-normal range is characterised by identifying the maximum gradient of the one-point AM coefficient and the peak-to-peak value of the two-point AM coefficient map.

Keywords: pipe flow; inter-scale interaction; amplitude modulation; two-point correlation; high Reynolds number

1. Introduction

1.1. Background

Pipe flows at high friction Reynolds numbers have received increasing attention over the past few decades in order to answer outstanding fundamental questions concerning scaling and modelling of wall-bounded turbulent flows [1, 2]. The friction Reynolds number is defined as $Re_\tau = \delta U_\tau/\nu$, where δ is the characteristic geometrical length of the outer scale, U_τ is the friction velocity and ν is the kinematic viscosity. An example of phenomena emerging only at high Reynolds number is the development of an outer peak in the spectrogram of the streamwise fluctuation u [3]. A similar scenario occurs in laboratory boundary layers (BL) [4, 5, 6], near-neutral atmospheric surface layers (NASL) [7, 8, 9, 10], channel (CH) flows [6, 11] and pipe flows [12, 13]. This is believed to be connected to the so-called large-scale coherent structures, i.e. coherent motions extending over scales larger than the outer length scale of the flow (e.g. pipe radius, channel half-width, or boundary layer thickness). Coherent structures have become the object of multiple studies due to their key role in mass, momentum and heat transfer [2, 14, 15, 16, 17]. The coherent motions can be divided into small-scale turbulence, large-scale-motions (LSM) [6, 18, 19], and very-large-scale-motions (VLSM) [5, 20, 21, 22] according to their streamwise extent scaled with the outer length scale δ. The characteristic wavelength of VLSMs in internal flows is $\sim 10\delta$ [23], while it is $\sim 6\delta$ in BLs [24].

At high Re_τ, the nonlinear inter-scale interaction between large and small scales adds complexity to the dynamics of coherent structures. Bandyopadhyay & Hussain [25] explored the universality of large- and small-scale coupling in turbulent shear flows and noted a phase reversal at the edge of the log layer in boundary layers. Hutchins & Marusic [24] studied the scale interaction through a scale

Email address: ye.li@sjtu.edu.cn (Ye Li)

decomposition of u obtained from hot-wire measurements, and termed the nonlinear modulating influence of large scales as amplitude modulation (AM). Mathis et al. [26] further quantified the AM effect through the correlation between the large-scale component and the envelope of the small-scale component extracted by Hilbert transformation, and developed a predictive model of the near-wall turbulence for wall-bounded turbulent flows given only the large-scale outer-region information [27, 28, 29]. Although the AM effect was captured by the one-point AM correlation coefficient at zero time-delay between scales [26], Schlatter & Örlü [30] raised that this coefficient is strongly related to the local skewness factor even in artificial signals, thus questioning the genuine physical interpretation of the results. To overcome this, Pirozzoli & Bernardini [31] constructed the two-point AM co-variance map as a refined measure of the inner-outer interaction and applied this analysis to direct numerical simulation (DNS) data of a supersonic BL. Baars et al. [32] studied effects of AM and frequency modulation by replacing the envelope of small-scale fluctuations in two-point correlations, with two time series of instantaneous amplitude and frequency of small scales derived from wavelet power spectrum. Dogan et al. [33] recently reviewed various methodologies of scale decomposition and AM quantification.

While these studies have clearly established that a certain degree of AM occurs in the wall-bounded flows, the physics behind this inter-scale interaction is still an open question. Hunt & Morrison [34] proposed the 'top-down' instability at high Re_τ opposed to the 'bottom-up' mechanism common in lower-Re_τ studies, based on both laboratory and field BL data. Guala et al. [35] noted that the scale separation achievable in NASL at high Re_τ is the key for their observations of VLSMs coexisting and interacting with structures from the hairpin paradigm. Baars et al. [36] found the AM effect in a confined domain centred on the internal shear layers of the large-scale uniform momentum zones, and revealed the transition from near-wall modulation to intermittent-type scale arrangement in the log-region of the BL. Agostini & Leschziner [37] concluded that the modulation in the skin friction does not reflect a direct interaction between small and large scales, but arises from variations in shear-induced production due to changes in the conditional velocity profile. The newly developed quasi-steady-quasi-homogeneous theory stated that the small-scale near-wall motions adapt to the large-scale fluctuations of the wall shear stress, which was found to perform better for Reynolds number $Re_\tau > 950$ and wall-normal distance $y^+ < 70$ on the basis of CH DNS data by Chernyshenko [38]. Despite significant efforts, the exact modulation mechanism and its dependence on the Reynolds number and flow configurations (e.g. BL, CH and pipe) are still largely unclear, and are the object of recent investigations, e.g. the study via complex networks by Iacobello et al. [39].

To this end, high-Re_τ data are extremely important since increasingly high Re_τ allows adequate scale separation, which facilitates an unambiguous identification of large-scale structures in the outer region and their influence on near-wall small-scale fluctuations. However, accurate measurements of the small scales become extremely difficult at high Reynolds number because of spatial resolution issues [40], and there are only a few experimental facilities that are designed to overcome this limit. One of these facilities is the long pipe of the 'Center for International Cooperation in Long Pipe Experiments' (CICLoPE). The size of small-scale turbulence within this pipe is enlarged by increasing the pipe radius R up to 0.45 m [41, 42]. Thanks to its large size, this facility covers the friction Reynolds number range of $4000 < Re_\tau < 60000$ while maintaining the viscous length scale (i.e. the inner length scale ν/U_τ) larger than 10 μm. This allows to accurately resolve high-Re_τ flow features by using conventional hot-wire probes and particle image velocimetry [13, 43, 44, 45, 46].

1.2. Research objectives

Previous studies of the AM effect mainly focus on laboratory BLs or NASLs, and related studies on pipe flows at high Re_τ are still limited. Although Mathis et al. [47] presented a comparison of AM effects in BL, pipe flow and CH at matched Reynolds number of $Re_\tau \approx 3000$, more experimental results for pipe flows at higher Re_τ are valuable. In addition, the distinct intermittency of BLs and pipe flows may lead to different behaviours in the outer region. Hence, it is worth investigating the inter-scale interaction in the outer region of pipe flows, especially the typical feature of the phase difference between large-scale structures and small-scale fluctuations.

Taking advantages of the CICLoPE facility (high Re_τ and large ν/U_τ), two sets of hot-wire measurements are performed to provide new insights on the features of coherent structures and of the inter-scale effect in turbulent pipe flows at Re_τ up to 40000. In the first set, a rake of five probes is used to obtain streamwise velocity measurements at five wall-normal positions simultaneously. Simultaneous signals allow to investigate the influence of the wall-normal location on two-point correlation maps. In the second set, a single probe has been used to scan the whole pipe radius. After validating the basic geometric features of correlated coherent structures and discussing the scale-dependence, one-point and two-point maps of the AM correlation are presented and compared to study the inter-scale interaction, including the phase relation and the correlation intensity, as well as the Re_τ effect. The details of the hot-wire experimental measurements in CICLoPE are firstly presented in § 2. Then the results of correlation maps, geometric features of coherent structures and their scale-dependence are reported in § 3. The inter-scale modulation is discussed in § 4 and, finally, the paper is concluded in § 5.

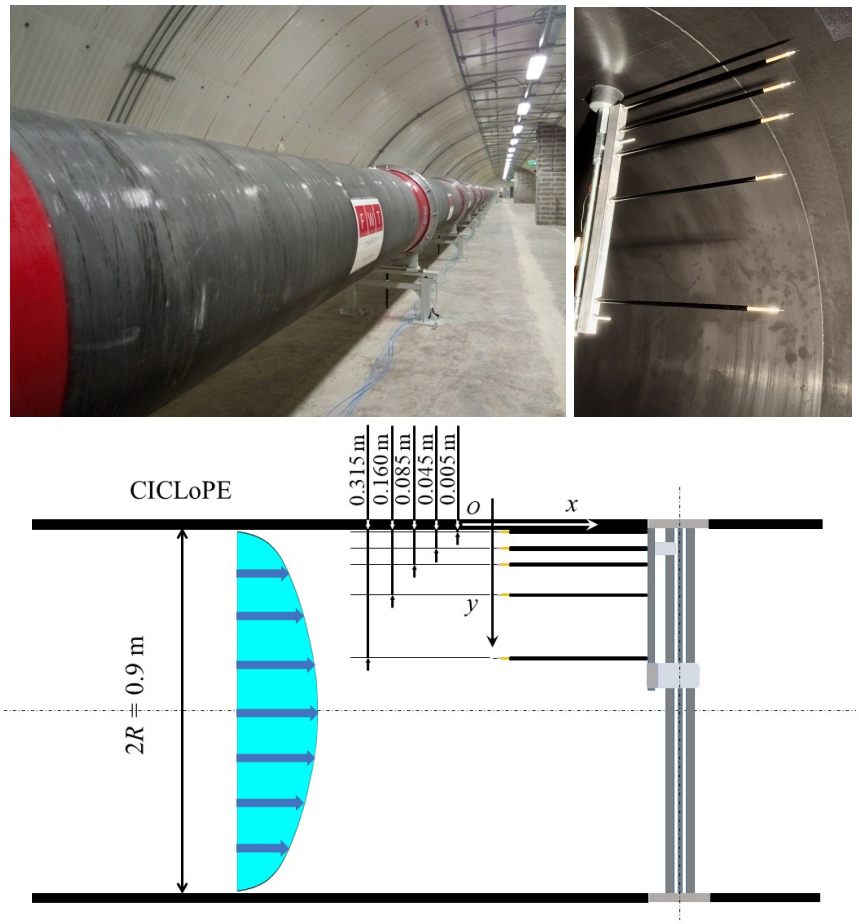

Figure 1: Experimental setup. Top-left: picture of the test section of CICLoPE; top-right: picture of the hot-wire rake mounted on the traversing system; bottom: schematic diagram of the rake installed in the pipe.

2. Experimental set-up

2.1. CICLoPE facility and flow field

The long pipe wind tunnel of CICLoPE is a closed-loop circuit operating with air at atmospheric pressure. The test section is 111.5 m long with an inner radius R of 0.45 m. The length-to-diameter ratio of approximately 124 ensures fully-developed turbulent flows at the downstream measuring location. For further details about the CICLoPE facility, refer to [41, 42, 43, 48].

Reynolds numbers in the range $7800 \leqslant Re_\tau < 40000$ are achieved by varying the incoming-stream velocity. The friction Reynolds number can be interpreted as the ratio of the outer length scale over the inner length scale, $Re_\tau = R/(\nu/U_\tau)$. With the large outer length scale of $R = 0.45$ m, the viscous length scale ν/U_τ remains larger than 11 μm as Re_τ increases up to 40000 thus it is possible to perform accurate turbulence measurements with standard hot-wire probes [49].

Specific values of characteristic quantities of the present pipe flows are listed in table 1. At the measuring station, air flow density ρ and kinematic viscosity ν are obtained according to the ideal gas law and the Sutherland law, by monitoring ambient pressure and air flow temperature. The centerline velocity $U_{\rm cl}$ is measured by a Prandtl tube connected to a high-accuracy differential pressure transducer, with a total uncertainty smaller than 0.16%. Static pressures along the pipe length are acquired by a digital multipoint pressure scanner Initium. The streamwise pressure gradient is calculated by fitting static pressures within the last 40 m before the measuring station to provide an estimate of wall shear stress $\tau_{\rm w}$ according to $\tau_{\rm w} = -{\rm d}P/{\rm d}x \cdot R/2$. The friction velocity $U_\tau = \sqrt{\tau_{\rm w}/\rho}$ is obtained within an estimated uncertainty of 0.06% [50]. The bulk velocity in the test section $U_{\rm b}$ is obtained within an uncertainty of 0.05% by using the pressure drop along the contraction section whose contraction ratio is 4.

2.2. Hot-wire measurements

By means of a hot-wire rake, we acquired synchronised time series of streamwise velocity at five different radial locations for four different Reynolds numbers, namely $Re_\tau = 7800, 9700, 20000, 39300$. The rake consisting of five single-wire probes was placed at about $x/D = 123$ downstream the outlet of the contraction section, with probes mounted at $y/R = 0.01, 0.10, 0.19, 0.36, 0.70$ as illustrated

Re_τ	U_b (m/s)	U_τ (m/s)	ν/U_τ (μm)	f_s (kHz)	T (s)	l^+	Δt^+	TU_cl/R	
7800	6.23	0.27	57.4	10	1200	17	0.46	20100	
9700	8.16	0.33	46.4	10	1300	22	0.71	27700	probe rake
20000	18.3	0.68	22.5	20	700	44	1.51	32400	
39300	37.7	1.34	11.4	20	700	87	5.85	65400	
32000	28.9	1.07	14.1	60	100	71	1.27	7200	single probe

Table 1: Experimental conditions and HWA acquisition settings.

in figure 1. A wall-normal well-resolved streamwise velocity profile at $Re_\tau = 32000$ was also measured by traversing a single-wire probe along the pipe radial direction. To measure the near-wall region with fine separation, a relative optical linear encoder was utilised.

The hot-wire probes were home-made with fully-etched Platinum Wollaston wires (5 μm nominal diameter) soft-soldered to conical steel prongs [51]. The length of sensitive wires l was 1 mm and the wire aspect ratio l/d was 200. Carbon-fibre probe holders were used to reduce the effect of mechanical vibrations on the measurements. Hot-wires were operated through a constant-temperature anemometer module at a resistance overheat ratio of 70%. Measurements for different Re_τ were taken with properly set sampling frequencies f_s and recording times T (see details in table 1). To avoid aliasing, low-pass filters were used prior to data acquisitions and cut-off frequencies were set according to the Nyquist theorem. Pre/post-calibrations exhibited a mild drift, and a linear interpolation between them was used to correct for the drift during the course of the experiment [52].

The resultant spatial and temporal resolutions of the hot-wire measurements (see the inner scaled sensitive wire length l^+ and sampling time interval Δt^+ in table 1) are acceptable to support the following correlation-based analysis, including the calculation of AM coefficients. With increasing Re_τ, both viscous length- and time-scales decrease, which leads to a poorer spatial and temporal resolution for measurements at $Re_\tau > 20000$ [53]. However, energy attenuation due to the reduction of spatial and temporal resolutions mainly occurs at the small-scale end, while the large scales are almost unaffected. Moreover, the attenuation is mainly in the inner region of the wall-bounded flows, so the introduced errors are relatively small at the present measuring points. By using the correction formula for streamwise broadband Reynolds stress [54], the relative errors are not larger than 3% at $y/R = 0.01$ and gradually attenuate to less than 0.3% at $y/R \geqslant 0.10$ in the highest-Re_τ case.

3. Correlations, coherent structures and scales

Streamwise velocities at five wall-normal locations are temporally resolved by the hot-wire rake, and recorded for four Re_τ cases. On this basis, two-point correlation maps are presented with different reference probe locations, showing Re_τ independence with the outer scaling. Furthermore, the scale dependence of the two-point correlation is discussed by using orthogonal discrete wavelet analysis of streamwise velocity fluctuations.

3.1. Two-point correlation maps

The spatial-temporal two-point correlations have revealed geometric features of the dominant coherent structure in BLs at relatively low Re_τ as reviewed by Hutchins & Marusic [5]. Accordingly, full-scale streamwise velocity correlation maps in the streamwise and wall-normal plane of the pipe flow at Re_τ up to 40000 are presented in this subsection.

The correlation function of the streamwise velocity fluctuation u at the wall-normal reference position y_r with u at y is defined as

$$R_{uu}(y_\mathrm{r}, y, \tau) = \langle u(y_\mathrm{r}, t)u(y, t-\tau)\rangle, \tag{1}$$

where τ is the time-delay and angle brackets indicate time averages. Note that $\tau > 0$ ($\tau < 0$) indicates that the correlated u is located downstream (upstream) with respect to the reference u. Based on the correlation function, we can define the correlation coefficient as

$$\rho_{uu}(y_\mathrm{r}, y, \tau) = \frac{\langle u(y_\mathrm{r}, t)u(y, t-\tau)\rangle}{\sigma_u(y_\mathrm{r})\sigma_u(y)}, \tag{2}$$

where σ_u is the standard deviation of u. The correlation function and coefficient describe the statistical intensity and coherence, respectively, over a wall-normal range for coherent structures with core located at y_r. The normalised correlation function ratio $R_{uu}(y_\mathrm{r}, y, \tau)/R_{uu}(y_\mathrm{r}, y_\mathrm{r}, 0)$ and the coefficient $\rho_{uu}(y_\mathrm{r}, y, \tau)$ are compared in figure 2 for different reference positions y_r/R and for a range of Reynolds numbers. These two quantities are scaled differently, the former with the zero-delay auto-correlation, i.e. the standard deviation of the reference u, while the latter with the standard deviations of both the correlated and the reference u signals. In these results, τ is scaled by using the pipe radius R and the convection velocity U_c which is set as the mean velocity at the reference point U_r or the bulk velocity U_b as specified.

In the left column of figure 2, iso-value regions with different $R_{uu}(y_\mathrm{r}, y, \tau)/R_{uu}(y_\mathrm{r}, y_\mathrm{r}, 0)$ levels extend in both wall-normal and streamwise directions, when the reference

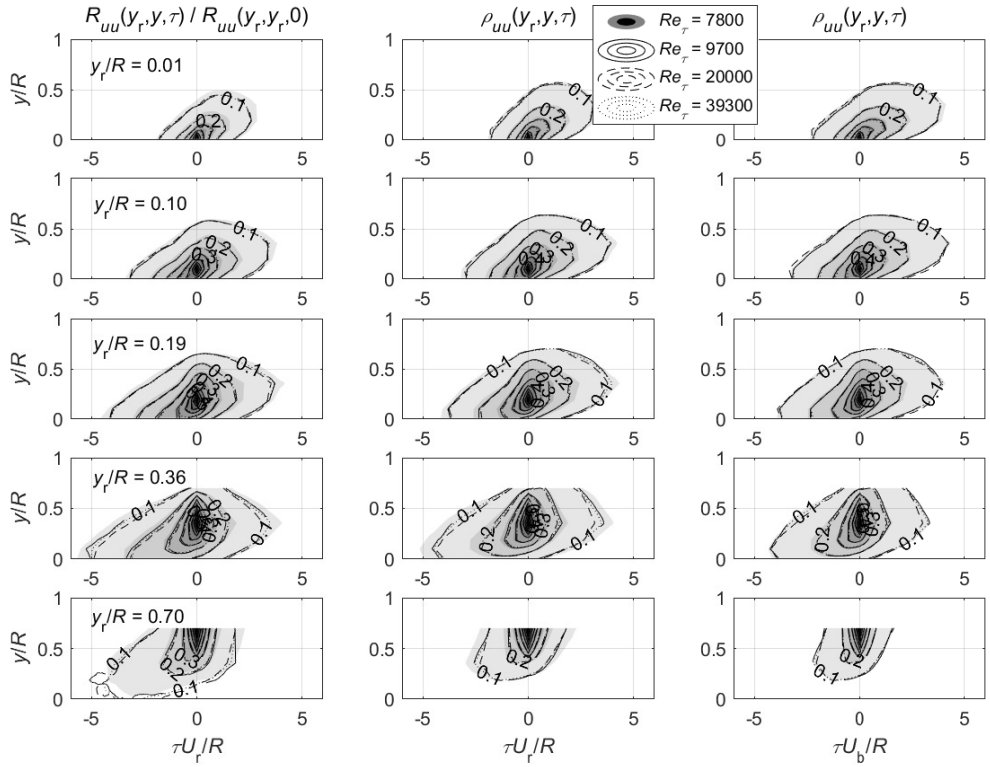

Figure 2: Contours of $R_{uu}(y_\mathrm{r}, y, \tau)/R_{uu}(y_\mathrm{r}, y_\mathrm{r}, 0)$ (left column) and $\rho_{uu}(y_\mathrm{r}, y, \tau)$ (middle and right columns) with contour-levels of 0.1:0.1:0.9. $U_\mathrm{c} = U_\mathrm{r}$ (left and middle columns) and $U_\mathrm{c} = U_\mathrm{b}$ (right column). $y_\mathrm{r}/R = 0.01, 0.10, 0.19, 0.36, 0.70$ from top to bottom. Shadow filled contour, solid, dashed and dotted lines respectively for $Re_\tau = 7800, 9700, 20000, 39300$.

point moves away from the wall towards the upper bound of the log layer. Beyond $y_\mathrm{r}/R \geqslant 0.19$, different trends of the spatial extent with increasing y_r/R are observed for regions with strong ($\geqslant 0.3$) and weak ($\leqslant 0.2$) correlation levels. On one hand, while the weak correlation regions still extend slightly upstream, the strong correlation regions begin to shrink progressively until $y_\mathrm{r}/R = 0.7$. On the other hand, the strong correlation regions show a symmetric feature with increasing y_r/R, while the weak correlation regions keep the asymmetric feature of the upstream tail at low y/R. In addition, the weak correlation regions begin to detach from the wall only for $y_\mathrm{r}/R = 0.7$, while the strong correlation regions start to gradually detach for lower y_r/R values. Contours of $\rho_{uu}(y_\mathrm{r}, y, \tau)$ in the central column of figure 2 look similar to those of $R_{uu}(y_\mathrm{r}, y, \tau)/R_{uu}(y_\mathrm{r}, y_\mathrm{r}, 0)$, but their local sizes differ both in the streamwise and wall-normal directions. The reason behind this difference is the normalisation of $\rho_{uu}(y_\mathrm{r}, y, \tau)$, where not only $\sigma_u(y_\mathrm{r})$ but also the monotonically-decreasing $\sigma_u(y)$ are used. The influence of the convection velocity is also shown in figure 2 (U_r in the central column and U_b in the right column), and it is seen to affect the converted streamwise extent of the iso-value regions. Given that U_b is a global quantity and has larger values than U_r in the inner region, a larger extent of $\tau U_\mathrm{b}/R$ is observed.

Correlation maps in each plot have well overlapped contours for pipe flows in the range of $7800 \leqslant Re_\tau < 40000$, implying the Re_τ independence of two-point coherence and geometric features (e.g. inclination angles and length scales) of the u-bearing coherent structures [22, 55]. These correlation maps are qualitatively similar to those of BLs and CHs at matched reference locations [22, 56]. On one hand, the typical correlated regions inclined towards the downstream direction are observed in the different flow configurations. The present inclination angle, which is derived from the correlation coefficient peak with the reference point located at $y_\mathrm{r}/R = 0.01$, is of $15.2° \pm 0.6°$ and is very close to the invariant value found by Marusic & Heuer [56]. On the other hand, when the reference point moves away from the wall to $y_\mathrm{r}/R \leqslant 0.25$, the correlation maps of these flows are found to cover larger areas according to the DNS results of BL and CH by Sillero et al. [22]. By integrating the correlation coefficient and converting the time-delay to streamwise length, the integral scale L_x^I is extracted and compared with the literature of CHs and BLs in figure 3. The resulting streamwise integral length scale of pipe flows increases with a logarithmic trend for $y_\mathrm{r}/R \leqslant 0.15$ and decreases quickly for $y_\mathrm{r}/R \geqslant 0.3$. L_x^I is basically unaffected by Re_τ, whereas differences are found

among the different flow configurations. In the log region, the present integral length values are more comparable to those measured for CHs by Monty [57], both larger than those for BLs by Pirozzoli & Bernardini and Sillero et al. [22, 31].

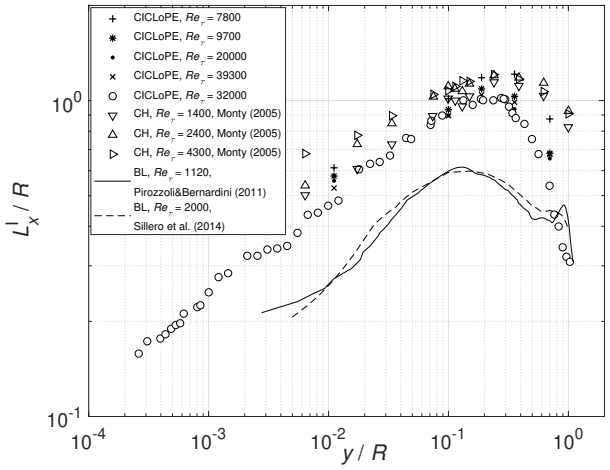

Figure 3: Profiles of L_x^{I}/R versus y/R in CICLoPE at $Re_\tau = 7800, 9700, 20000, 39300, 32000$ $(+, *, \cdot, \times, \circ)$, compared with results in CHs by Monty [57] at $Re_\tau = 1400, 2400, 4300$ $(\triangledown, \triangle, \triangleright)$ and in BLs by Pirozzoli & Bernardini [31] (solid line) and Silliero et al. [22] (dashed line).

3.2. Scale decomposition

Scale decomposition is a prerequisite to present the scale dependence of coherent motions and to further study the scale interaction. Compared to commonly used Fourier transform with fine frequency resolution, the wavelet transform allows the analysis of turbulent flows in terms of both time and scale, up to the limits of the uncertainty principle [58]. The translated and/or dilated wavelets fit well with self-similar coherent structures in wall-bounded turbulent flows. Orthogonal discrete wavelet transform (ODWT) with a fast algorithm similar to the fast Fourier transform, i.e. Mallat pyramidal algorithm [59], is applied to decompose scales and to reconstruct large- and small-scale velocity components for the AM correlation. Here, we note the following features of this methodology. On one hand, Butterworth filters are not used, because they are typical IIR digital filters with nonlinear phase response [60], which may introduce an uncertain phase difference between decomposed large- and small-scale components. By contrast, the ODWT-based filtering has a better phase response. In comparison with original signals, decomposed large-scale components by the ODWT-based filtering are found to perform smaller phase differences than those by Butterworth filters. This gives the confidence to the analysis on the phase shifts in the AM correlation map by using ODWT. On the other hand, ODWT is different from the continues wavelet transform used by Baars et al. [32]. Baars et al. adopted the Morlet wavelet and the Mexican-hat wavelet as the mother wavelet, which only satisfies the admissibility condition of continuous wavelet but not the orthogonality condition. The resulting wavelet coefficients would produce energy redundancy and the discrete small- and large-scale velocity components would not be available. In this paper, ODWT produces the scale-decomposed velocity components with no energy redundancy.

In the practical implementation, we choose the 5th order Daubechies wavelet for its compact support, regularity and relatively high vanishing moments. A raw time series of streamwise velocity is decomposed into a total of 20 wavelet modes. The scale of each wavelet mode and its characteristic frequency are linear-log related [61]. After the decomposition, wavelet energy spectra E_{uu}^{w} of all the modes are calculated by integrating individual modes over the time domain. Note that E_{uu}^{w} are equivalent to the frequency-premultiplied Fourier spectra, and the sum of E_{uu}^{w} over all the modes is equal to the variance of u, with a very small energy redundancy due to numerical errors. It is also noted that E_{uu}^{w} as well as other scale-decomposition-related results are almost unaffected by choosing different wavelet bases [32, 61]. The results of E_{uu}^{w} at $Re_\tau = 32000$ are shown in figure 4.

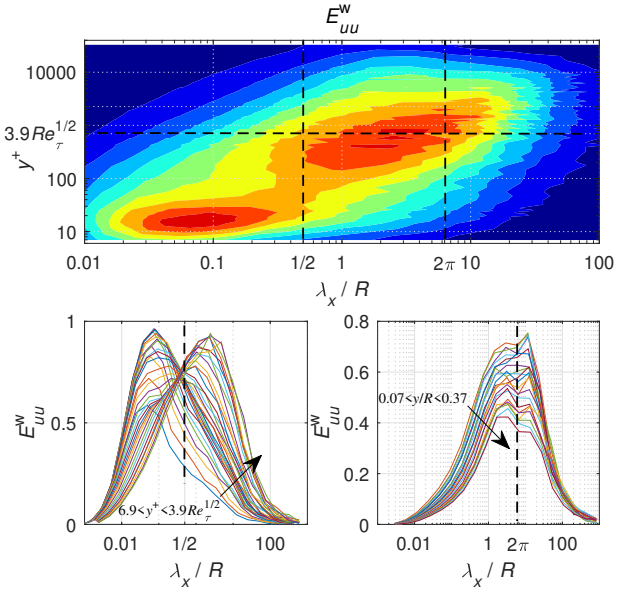

Figure 4: Top: contours of $E_{uu}^{\mathrm{w}}(\lambda_x/R, y^+)$ with contour-levels of 0(dark blue):0.1:0.9(dark red); wall-normal location of OSP (horizontal dashed line), and wavelengths of $\lambda_x/R = 1/2, 2\pi$ (vertical dashed lines). Bottom: E_{uu}^{w} versus λ_x/R for $6.9 < y^+ < 3.9\sqrt{Re_\tau}$ (left) and $0.07 < y/R < 0.37$ (right). $U_{\mathrm{c}} = U_{\mathrm{r}}$ at $Re_\tau = 32000$.

A closer look at the spectra in the top panel reveals the presence of two well-separated peaks: the inner and the outer spectral peaks (marked as OSP from here on).

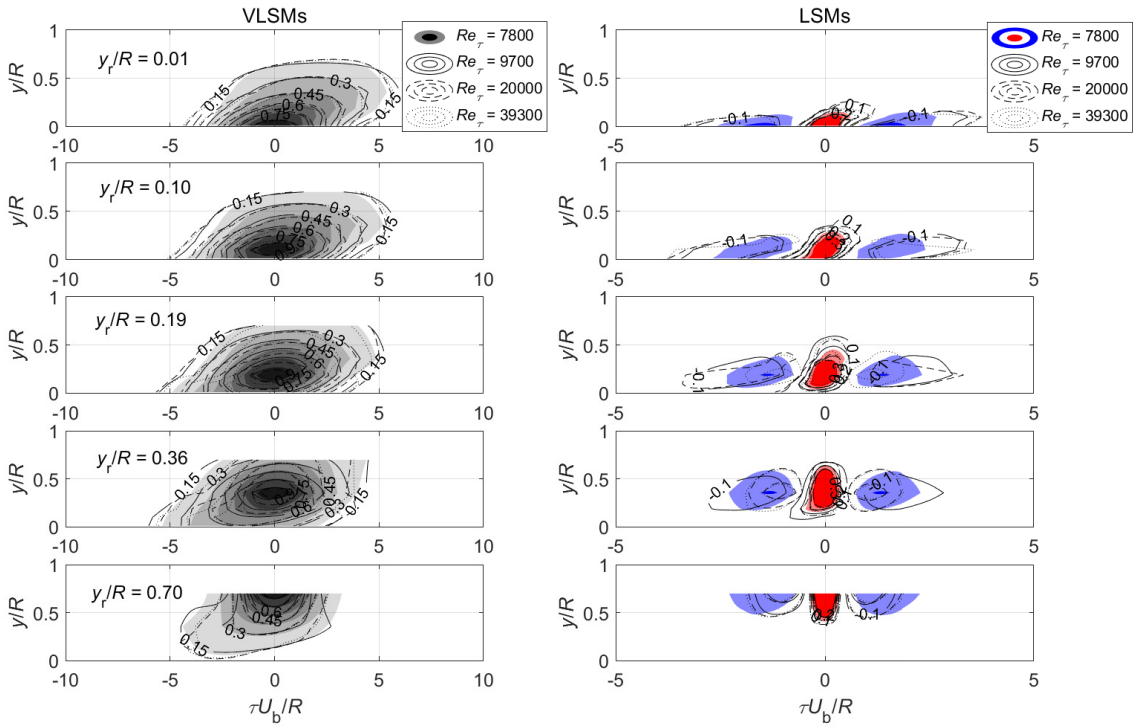

Figure 5: Contours of $\rho_{u_{\rm vl}u_{\rm vl}}(y_{\rm r}, y, \tau)$ (left, VLSMs) and $\rho_{u_{\rm l}u_{\rm l}}(y_{\rm r}, y, \tau)$ (right, LSMs). $y_{\rm r}/R = 0.01, 0.10, 0.19, 0.36, 0.70$ from top to bottom. Shadow filled contour, solid, dashed and dotted lines respectively for $Re_\tau = 7800, 9700, 20000, 39300$. Contour-levels of 0.15:0.15:0.9 (left) and -0.3:0.1:0.3 (right, no zero level for clarity, positive in red and negative in blue). $U_{\rm c} = U_{\rm b}$.

OSP is located at about $y^+ = 3.9\sqrt{Re_\tau}$ [26]. According to the wavelength analysis of the inner and outer spectral peaks by Fiorini [50] and to the $E^{\rm w}_{uu}$ curves in the wall-normal range of $6.9 < y^+ < 3.9\sqrt{Re_\tau}$ shown in the left-bottom panel of figure 4, the cut-off wavelength of $\lambda_{\rm c}/R = 1/2$ is appropriate to separate the small- and large-scale motions over the Reynolds number range available in CICLoPE. The right-bottom panel of figure 4 shows $E^{\rm w}_{uu}$ in terms of the outer scaled streamwise wavelength λ_x/R for $0.07 < y/R < 0.37$. A bi-modal distribution is observed with one peak located at $\lambda_x/R \approx 3$ and the other at $\lambda_x/R \approx 10$. In the interval of $3 < \lambda_x/R < 10$, we achieve a boundary reference $\lambda_x/R = 2\pi$ passing through troughs between two peaks in the bi-modal distribution. With this cut-off wavelength, the wavelet spectral contents of VLSMs and LSMs are considerable. Considering the results by Bailey & Smits [21], intensities of the scale-decomposed correlations are affected by the choice of the cut-off wavelength, but the characteristic spatial scales of those correlations are largely unaffected. In addition, it is noted that as y/R increases further into the wake region, the two-peak structure of the spectra gradually disappears. In the wake region, the spectral peak corresponding to LSMs dominates again and the relative energy contained by VLSMs decreases.

Time series of streamwise velocities for VLSMs and LSMs, respectively referred to as $u_{\rm vl}$ and $u_{\rm l}$, are reconstructed by superposing wavelet modes whose streamwise wavelengths fulfil the requirements of $\lambda_x/R > 2\pi$ for VLSMs and $1/2 < \lambda_x/R < 2\pi$ for LSMs. The correlation coefficient maps of $\rho_{u_{\rm vl}u_{\rm vl}}$ and $\rho_{u_{\rm l}u_{\rm l}}$ in figure 5 show geometric properties of the VLSMs and LSMs. Compared with the full-scale correlation maps plotted in figure 2, the correlation maps of the VLSMs show similar geometry, but the correlation maps of the LSMs are largely different. In the left column, the VLSMs maintain similarity for $y_{\rm r}/R \leqslant 0.36$ and show $\Delta y (= y - y_{\rm r})$-independence [21]. The weak coherence region with the contour-level of 0.15 shows quasi-linear variations of the streamwise scales with y in both the upstream and downstream directions, which manifests as the vertical coherence [22, 55]. The vertical coherence makes the VLSMs (mainly populating the outer region) extending into the near-wall region. The VLSMs bear the mean shear over a wide wall-normal range, especially the strong shear near the wall, leading to the shown inclination. The right column of figure 5 shows that the LSMs do not present the long-tail feature as the VLSMs, but show the local coherence feature, i.e. one positively correlated region flanked by upstream and downstream negatively correlated regions. The LSMs are practically symmetrical in the wake region, but show inclined contours of $\rho_{u_{\rm l}u_{\rm l}} \neq 0$ in the inner region, due to the strong

wall shear. A closer check of these correlation maps over the range of $7800 \leqslant Re_\tau < 40000$ reveals the Re_τ effect on the LSMs and VLSMs. Although a certain degree of Re_τ similarity is observed, the correlation maps of the LSMs and VLSMs, at different Re_τ, do not collapse as well as those of the full-scale motions, meaning a worse Re_τ-invariance despite the same normalisation. It is worthy of further study whether the Re_τ effects are physical or caused by the choice of the cut-off wavelength used to separate the LSMs and VLSMs.

4. Inter-scale interaction

The interaction between inner and outer regions of turbulent wall-bounded flows possibly involves both linear and nonlinear mechanisms [24, 27]. The linear mechanism is the superimposition of large scales, populating the log layer, onto near-wall small scales. One of the nonlinear mechanisms can be identified as amplitude modulation. The AM effect is quantified by the two-point cross-correlation between the large-scale component of the streamwise velocity at location 1 (i.e. the reference location y_r), $u_{1\mathrm{L}}$, and the low-pass filtered envelope of small-scale streamwise fluctuations at location 2, $u_{2\mathrm{EL}}$ [26]. AM function is defined as

$$R^{12}_{\mathrm{AM}}(\tau) = \langle u_{1\mathrm{L}}(t) u_{2\mathrm{EL}}(t-\tau) \rangle, \tag{3}$$

and AM coefficient is defined as

$$\rho^{12}_{\mathrm{AM}}(\tau) = \frac{\langle u_{1\mathrm{L}}(t) u_{2\mathrm{EL}}(t-\tau) \rangle}{\sigma_{u_{1\mathrm{L}}} \sigma_{u_{2\mathrm{EL}}}}, \tag{4}$$

where σ_A is the standard deviation of A. The large- and small-scale components are separated by the ODWT-based filtering, and the envelope of small-scale fluctuations is extracted by means of the Hilbert transform. As discussed in section 2.2, resolution issues of hot wires mainly occur as the small-scale attenuation. This attenuation is simulated by discarding the small-scale energy with different streamwise wavelengths. AM correlations in the case of discarding with $\lambda_x^+ < 2400$ are basically the same with AM correlations in the case without discarding. The comparison implies that AM correlations are nonsensitive to the resolution issues. Two distinct regions respectively corresponding to the AM effect and an opposite AM effect are noted in both one- and two-point AM maps, which show Re_τ independence in the range of $7800 \leqslant Re_\tau < 40000$. Details of AM and opposite effects are discussed in regard of the wall-normal location and time-delay.

4.1. One-point AM correlation

As argued by Mathis et al. [26], the one-point AM coefficient ρ^{11}_{AM} at zero time-delay ($\tau = 0$) between large and small scales can be treated as a reasonable estimate of the AM effect. $\rho^{11}_{\mathrm{AM}}(\tau = 0)$ is found analogous to $\overline{u_L u_S^2}$ which is the only Re_τ-dependent term among the scale-decomposed skewness factors [62]. In order to study effects

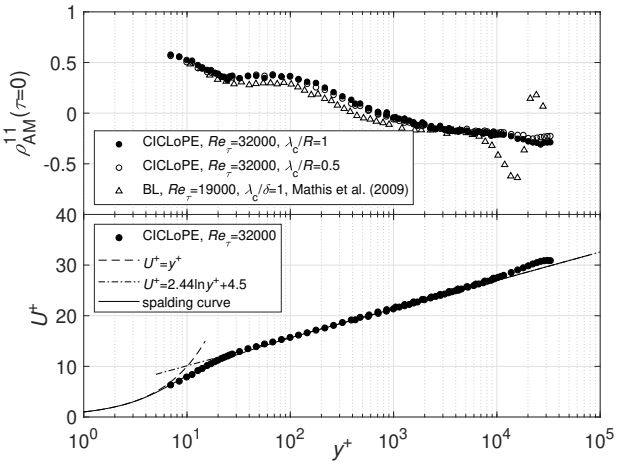

Figure 6: Top: profile of $\rho^{11}_{\mathrm{AM}}(\tau = 0)$ versus y^+ with $\lambda_\mathrm{c}/R = 1, 1/2$ (• and ∘) in CICLoPE at $Re_\tau = 32000$, compared with the BL at $Re_\tau = 19000$ by Mathis et al. [26] (△). Bottom: profile of U^+ versus y^+.

of the Reynolds number and flow configuration on AM, we compare the wall-normal profile of $\rho^{11}_{\mathrm{AM}}(\tau = 0)$ in CICLoPE at $Re_\tau = 32000$ with that in the BL at $Re_\tau = 19000$ by Mathis et al. [26] in the top panel of figure 6. The trends of $\rho^{11}_{\mathrm{AM}}(\tau = 0)$ with y^+ are consistent in the inner region, which agrees with the comparison between BL, pipe and CH flows at $Re_\tau \approx 3000$ by Mathis et al. [47]. The sign change of $\rho^{11}_{\mathrm{AM}}(\tau = 0)$ from positive to negative in the two profiles occurs at approximately $y^+ = 3.9\sqrt{Re_\tau}$ where the centre of the log layer and the OSP are located. Moreover, two differences between these two profiles are observed. One is the upward shift of $\rho^{11}_{\mathrm{AM}}(\tau = 0)$ with Re_τ for $y^+ > 30$, because stronger large-scale structures, with increasing Re_τ, modulate the small-scale fluctuations more intensely. The other occurs in the wake region due to the different outer boundary conditions. In particular, the BL flows show strong intermittency in the wake region, which is manifested as a valley followed by a peak in the $\rho^{11}_{\mathrm{AM}}(\tau = 0)$ profile. However, the gradual change of $\rho^{11}_{\mathrm{AM}}(\tau = 0)$ in the wake region of the pipe flow indicates a weaker intermittency. For the same reason, the profile of the time-averaged streamwise velocities in the pipe flow does not depart from the log law too much in the wake region as shown in the bottom panel of figure 6. In addition, the choice of the cut-off wavelength λ_c only makes minor differences to $\rho^{11}_{\mathrm{AM}}(\tau = 0)$ at least in the range of $1/2 \leqslant \lambda_\mathrm{c}/R \leqslant 1$.

To further explore the one-point AM effect and the associated phase reversal, we extend the commonly used quantification of the wall-normal $\rho^{11}_{\mathrm{AM}}(\tau = 0)$ [26, 63] profile to the one-point AM correlation map on the plane spanned by the wall-normal distance and the time delay. Contours of the one-point AM function R^{11}_{AM} with levels

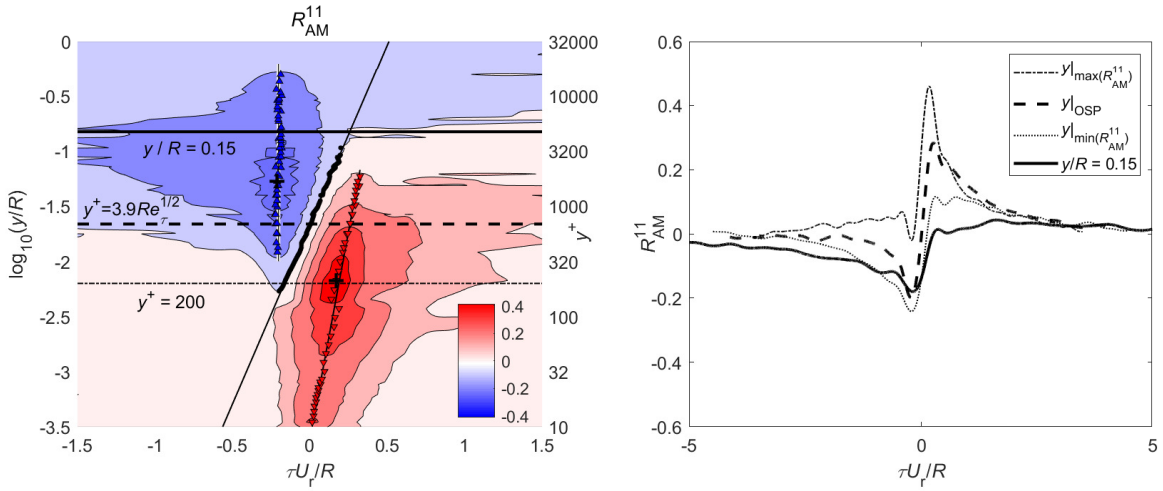

Figure 7: Left: contours of $R^{11}_{\rm AM}(\tau, \log y)$ with contour-levels of -0.2(dark blue):0.1:0.4(dark red); $R^{11}_{\rm AM} = 0$ marked with circles fitted by the inclined solid line; the maximum and the minimum of $R^{11}_{\rm AM}(\tau)$ marked with $\triangledown$ and $\triangle$; the maximum and the minimum of $R^{11}_{\rm AM}(\tau, \log y)$ marked with black crosses; the centre, upper and lower bounds of the log layer marked with horizontal dashed, solid and dash-dotted lines. Right: curves of $R^{11}_{\rm AM}(\tau)$ at $y|_{\max(R^{11}_{\rm AM})}$ (dash-dotted line), $y|_{\min(R^{11}_{\rm AM})}$ (dotted line), $y|_{\rm OSP}$ (dashed line) and $y/R = 0.15$ (solid line). $U_{\rm c} = U_{\rm r}$ at $Re_\tau = 32000$.

between -0.2 and 0.4 are reported in the left panel of figure 7. The horizontal axis indicates the time-delay τ, while the vertical axis represents the logarithmic distance from the wall $\log y$. Both are normalised with the outer-scale units. $\tau > 0$ ($\tau < 0$) indicates that the correlated small scales are located downstream (upstream) with respect to the large scales. Near-wall red contours of $R^{11}_{\rm AM} > 0$ represent the AM effect, i.e. large-scale high/low-momentum structures enhance/suppress small-scale fluctuations. In the near-wall region governed by the inner scaling, the scaled velocity fluctuation $u^+ = u/U_\tau$ has a fixed value. According to the quasi-steady description [29, 38], an increase of the large-scale velocity implies a larger inner velocity scale U_τ. To keep the fixed value of u^+, small-scale fluctuations are enhanced on the absolute scale. This leads to positive correlations for the AM effect. Another mechanism with $R^{11}_{\rm AM} < 0$, referred to as the opposite AM effect (or opposite effect for simplicity), is observed in the outer region. The negative correlation region is attributed to intermittently-existing two flow states close to the outer edge of wall-bounded flows, i.e. the non-turbulent zones with approximate incoming-stream velocity and very low turbulence intensity, and the turbulent bulges with lower mean velocity and high small-scale fluctuations.

Furthermore, in figure 7, the maximum and the minimum of $R^{11}_{\rm AM}$ at different wall-normal locations y are identified for $|R^{11}_{\rm AM}| > 0.1$, and are marked with red and blue triangles respectively. The high and low bounds respectively correspond to the AM effect and the opposite effect, and behave differently along with y.

The time-delay τ of the maximum $R^{11}_{\rm AM}$ is found to be linear with $\log y$

$$\tau U_{\rm r}/R = 0.133 \log(y/R) + 0.480, \qquad (5)$$

from $y^+ = 7$ to $y/R = 0.06$. Note that the maximum $R^{11}_{\rm AM}$ at $y^+ = 7$ is located at $\tau = 0$, implying a synchronisation of the large-scale velocity and the small-scale amplitude in the very-near-wall region. When moving far away from the wall, upstream large-scale structures in the outer region penetrate the near-wall region and induce downstream small-scale fluctuations by the AM mechanism. This phase relation of the one-point AM effect is consistent with the observation in the two-point AM map in the BL at $Re_\tau = 14750$ by Baars et al. [32] that the small-scale amplitude signal leads before the large-scale signature.

The anti-correlation occurs at an opposite time-delay which corresponds to the phase reversal phenomenon [25, 64] and the preferential scale arrangement [32, 65]. The normalised time-delay of the minimum $R^{11}_{\rm AM}$ is independent with y,

$$\tau U_{\rm r}/R = -0.202 \pm 0.002, \qquad (6)$$

meaning an almost fixed time-delay of the high/low small-scale fluctuation amplitude with respect to the low/high-momentum large-scale structures in the outer region. This fixed phase shift in the outer region in the pipe flow has yet not been observed from other studies. Considering the increase of $U_{\rm r}$ with y and the fixed value of $\tau U_{\rm r}/R$, the absolute value of τ and the inner-scaled value of τ^+ gradually vanish with y. This trend is consistent with the observation in the outer region of the BL by Baars et al. [32].

However, at the outer boundary, time-delay variations of the strongest opposite effect in the BL and the pipe flow are found to be different because of the distinguished intermittency in the wake region.

In the log layer, both the two mechanisms exist. The AM and opposite effects respectively occupy the right and left parts of the $\tau - \log y$ plane. The zero net-modulation with $R^{11}_{\rm AM} = 0$ separates two distinct regions where the inner AM effect and the outer opposite effect respectively dominate. The contour-line of $R^{11}_{\rm AM} = 0$ is also found to be linear in the log layer of $200 < y^+ < 0.15R^+$. By fitting the corresponding points marked with black circles, the relation between τ and y is obtained as

$$\tau U_{\rm r}/R = 0.307 \log(y/R) + 0.511. \tag{7}$$

In the near-wall region and in the wake region, the relation does not hold anymore. This contour-line is found to go through the point of $y^+ = 3.9\sqrt{Re_\tau}, \tau = 0$. It means that large-scale structures almost do not modulate small-scale fluctuations at the same phase at the wall-normal location close to the centre of the log layer (the location of OSP). The time-delay difference between the maximum modulation and the non-modulation,

$$\Delta\tau U_{\rm r}/R = -0.174 \log(y/R) - 0.031, \tag{8}$$

and the time-delay difference between the non-modulation and the minimum modulation,

$$\Delta\tau U_{\rm r}/R = 0.307 \log(y/R) + 0.713, \tag{9}$$

respectively characterise the periods of AM and opposite effects in the log layer. Although Baars et al. [32] focused on the effects in the BL while the present results are on the pipe flow, the above-mentioned time shifts, subject to the characteristic behaviours of AM and opposite effects, are in the similar trend with $\log y$. However, no such well-fitted linear-log relations as in this study were observed from their results. The wall-normal distributions of $U_{\rm r}$, $\sigma_{u_{\rm 1L}}$, and $\sigma_{u_{\rm 2EL}}$ could be the reason for this difference.

The maximum and the minimum in the whole $R^{11}_{\rm AM}$ map are marked with black crosses in figure 7. The maximum is located at $y^+ = 200$, which corresponds to the lower bound of the log layer as well as the opposite effect region. The minimum is at $y/R = 0.054$ and is close to the upper bound of the AM effect region. They are practically symmetrical about the centre of the log layer with zero time-delay, which is difficult to observe in the AM coefficient map by Baars et al. [32]. $R^{11}_{\rm AM}(\tau)$ curves at the two extreme locations, i.e. $y|_{\max(R^{11}_{\rm AM})}$ and $y|_{\min(R^{11}_{\rm AM})}$, are plotted in the right panel of figure 7 with $R^{11}_{\rm AM}(\tau)$ curves at $y|_{\rm OSP}$ and $y/R = 0.15$. $R^{11}_{\rm AM}$ at $y|_{\max(R^{11}_{\rm AM})}$ is nearly always positive over the time-delay domain. The curve at $y|_{\rm OSP}$ crosses the point with $\tau = 0$ and $R^{11}_{\rm AM} = 0$, and shows symmetry about this point. The tails of $R^{11}_{\rm AM}(\tau U_{\rm r}/R \geqslant 3)$ at varied y overlap well, but the tail with $\tau < 0$ is longer at $y/R = 0.15$. The four curves show a similar trend: a trough at negative τ followed by a peak at positive τ with $R^{11}_{\rm AM}$ increasing rapidly nearby $\tau = 0$. The troughs are located at approximately the same time-delay, $\tau U_{\rm r}/R = -0.2$. The absolute value of the minimum $R^{11}_{\rm AM}$ increases with y until $y|_{\min(R^{11}_{\rm AM})}$, then decreases. The value of the maximum, instead, decreases with y until the sharp single peak disappears at $y|_{\min(R^{11}_{\rm AM})}$.

Given that the AM and opposite effects coexist in the log layer, the compromise between two effects is further investigated based on the variation rate of the one-point AM coefficient with the time-delay, $\mathrm{d}\rho^{11}_{\rm AM}/\mathrm{d}\tau$. This quantity characterises the relative increase of the AM effect compared with the opposite effect. The maximum variation rate corresponding to the most rapid transition between the two mechanisms, and its corresponding time-delay are identified for varied y/R. The results are reported in figure 8. The value of $\mathrm{d}\rho^{11}_{\rm AM}/\mathrm{d}(\tau U_{\rm r}/R)$ decreases with y/R and follows a linear-log relation, $-0.73\log(y/R) + 0.12$, in the range of $-2.3 < \log(y/R) < -0.6$. This range corresponds to $160 < y^+ < 0.25R^+$ covering the whole log layer. Beyond $\log(y/R) = -0.5$, $\mathrm{d}\rho^{11}_{\rm AM}/\mathrm{d}(\tau U_{\rm r}/R)$ becomes stable at 0.5. The right panel of figure 8 shows the corresponding time-delay $\tau U_{\rm r}/R$. By regression, it is found that from the lower bound of the log layer to $y|_{\rm OSP}$ where $\log(y/R) = -1.66$,

$$\tau U_{\rm r}/R = 0.132 \log(y/R) + 0.267, \tag{10}$$

while beyond $\log(y/R) = -0.5$, the time-delay follows another law,

$$\tau U_{\rm r}/R = 0.133 \log(y/R) + 0.177, \tag{11}$$

which keeps the same slope but with an intercept shift of 0.09. This transition occurs in the upper half part of the log layer and the time-delay gradually increases with y/R but does not obey the linear-log relation. When y increases from $y|_{\rm OSP}$, the most rapid shift between the two effects is gradually moving from the AM-dominating region to the opposite-effect-dominating region. When y increases to $\log(y/R) = -0.5$, the phase reversal and the preferential scale arrangement gradually complete.

4.2. Two-point AM correlation

The global nonlinear effects of large-scale structures on small-scale fluctuations are discussed in this section. In order to remove the dependence from the local cross-term skewness factor [62] and to provide simultaneous information on the modulating and the modulated signals [31], we focus on the two-point AM correlation after checking the consistency with the one-point AM correlation. Compared to the previous analysis based on two-point hot-wire measurements [32], the present analysis considers the asymmetry of large and small scales in the AM correlation, and adopts large-scale structures at varied $y_{\rm r}/R$ and small-scale fluctuations at varied y/R based on the hot-wire measurements by a five-probe rake. This hot-wire

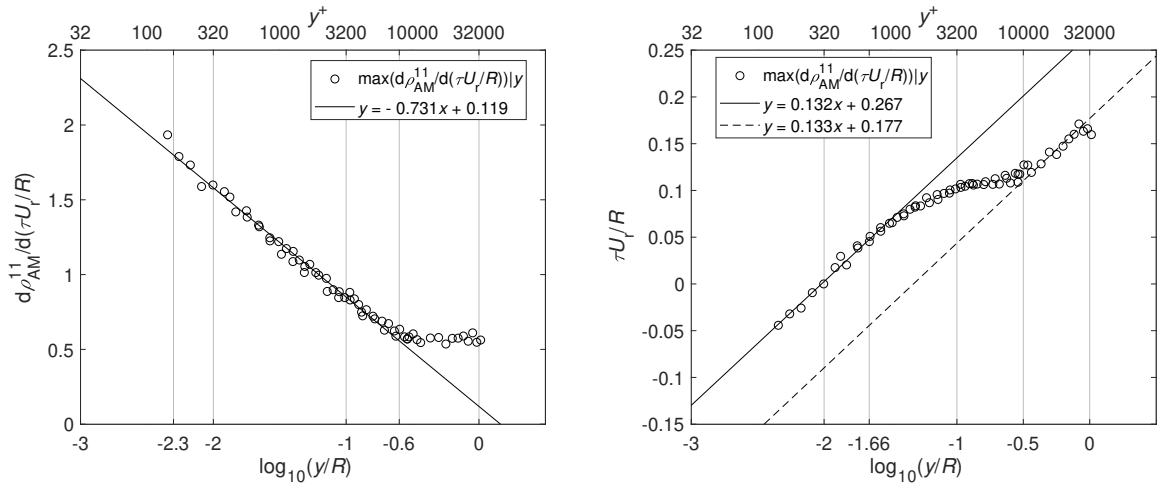

Figure 8: Profiles of the maximum $\mathrm{d}\rho^{11}_{\mathrm{AM}}/\mathrm{d}(\tau U_{\mathrm{r}}/R)$ (left) and the corresponding $\tau U_{\mathrm{r}}/R$ (right) versus $\log_{10}(y/R)$.

measurement setup also provides more details of negative two-point AM correlation in the outer region. Two-point AM coefficient maps are found to be independent of Re_τ but differ with increasing y_{r}/R. However, the outer-scaled time-delay of the strongest opposite effect stays unchanged.

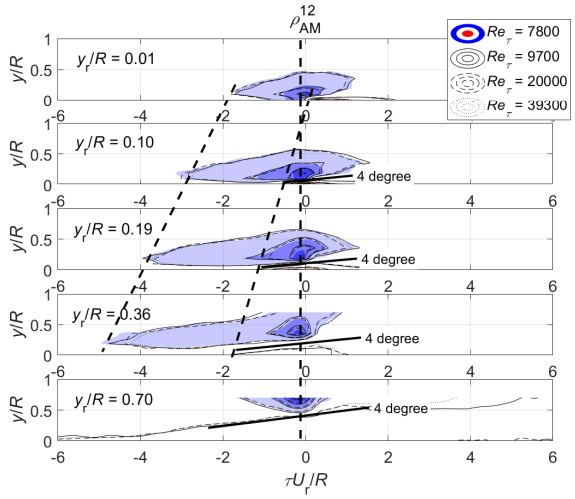

Figure 9: Contours of $\rho^{12}_{\mathrm{AM}}(\tau, y)$ with contour-levels of -0.3(dark blue):0.06:0.3(dark red) at $y_{\mathrm{r}}/R = 0.01, 0.10, 0.19, 0.36, 0.70$ from top to bottom. No zero level for clarity in the first 4 panels, positive in red and negative in blue. Shadow filled contour, solid, dashed and dotted lines for $Re_\tau = 7800, 9700, 20000, 39300$. $U_{\mathrm{c}} = U_{\mathrm{r}}$.

Consistent with the two-point AM function (R^{12}_{AM}) maps of BLs at $Re_\tau = 250, 500, 1120$ by Pirozzoli & Bernardini [31], the R^{12}_{AM} maps of pipe flows at $7800 \leqslant Re_\tau \leqslant 39300$ show increasing absolute intensity with Re_τ. However, from the two-point AM coefficient (ρ^{12}_{AM}) maps in figure 9, the Re_τ independence of ρ^{12}_{AM} is observed in the present Re_τ range. The AM region and the opposite effect region are respectively distributed in the right-bottom and left-top parts of the $\tau - y$ plane. The strongest opposite effect, i.e. the negative peak of $\rho^{12}_{\mathrm{AM}}(\tau, y)$ is found in the vicinity of $\tau = 0$, $y = y_{\mathrm{r}}$. These observations are also consistent with the results by Pirozzoli & Bernardini [31]. In addition, Pirozzoli & Bernardini noted that the positive peak at $y_{\mathrm{r}}/R = 0.2$ approximately leans in the positive 14 degree direction with respect to the reference point. We roughly estimate the inclination angle at $y_{\mathrm{r}}/R = 0.19$ for the pipe flows. A similar value of 13 degree is obtained. Another interesting inclination angle is also observed here. Contour-lines with $\rho^{12}_{\mathrm{AM}} = 0$ at different Re_τ are found to incline at about 4 degree with respect to the wall in the outer region, marked with thick solid lines in figure 9. This inclination angle is independent of y_{r}.

The $\rho^{12}_{\mathrm{AM}}(\tau, y)$ maps in figure 9 give richer spatial information than the one-point AM map. Regarding the wall normal range, the regions pertaining to the AM mechanism and the opposite effect behave differently when the reference point moves away from the wall. For the AM mechanism, small-scale fluctuations modulated by large-scale structures in the range of $y_{\mathrm{r}}/R \leqslant 0.19$, is limited to $y/R < 0.15$. The modulation ability of large-scale structures at larger y_{r} gradually attenuates. When y_{r}/R reaches 0.7, regions of $\rho^{12}_{\mathrm{AM}} > 0$ do not appear anymore, meaning that the above wall-normal range is completely dominated by the opposite effect. For the opposite effect, large-scale high-momentum motions carry low turbulence intensities, while low-momentum turbulent bulges carry larger small-scale fluctuations. The opposite effect maintained by large-scale structures at $y_{\mathrm{r}}/R = 0.01$ extends into the near-wall region for $Re_\tau < 20000$, prescribed that the upper bound of the near-wall region is at $y^+ = 200$. When y_{r}/R increases to 0.36, the wall-normal region influenced by the opposite effect goes away from the wall and

features larger wall-normal extents. At $y_r/R = 0.70$, not only the AM effect region disappears, but also the opposite effect region shrinks. As far as the streamwise range influenced by AM and opposite effects, the downstream ends do not change much for large-scale structures located in the range of $y_r/R \leqslant 0.19$. When y_r/R increases up to 0.36, the upstream ends of the weak AM effect region ($\rho^{12}_{\rm AM} = 0.06$) extend to $\tau U_r/R \approx -2$, while in the opposite effect region, large-scale structures even affect small scales at about $5R$ upstream. It is noted that the upstream ends of the opposite effect region are very close to the upstream ends of the velocity correlation maps (middle column of figure 2) for the same $y_r \leqslant 0.36$. It means that the weakest opposite effect occurs at the upstream edge of the large-scale structures.

Special attention is worth paying on the maximum and the minimum of $\rho^{12}_{\rm AM}$ in the whole $\tau - y$ plane. On one hand, the time-delay of the minimum $\rho^{12}_{\rm AM}(\tau, y)$, marked with a vertical dashed line in figure 9, shows a y_r independence, which is consistent with the fixed $\tau U_r/R$ of the opposite effect from the $R^{11}_{\rm AM}$ map. The strongest opposite effect is upstream of the centre of the large-scale structures, and the phase shift of small scales is far smaller than that with the weakest opposite effect. The small phase shift of the strongest opposite effect is argued to be maintained by intermittently-existing two flow states in the whole outer region, i.e. the non-turbulent zones and the turbulent bulges. In the non-turbulent zones (turbulent bulges), the weak (strong) turbulence intensity closely follows the high (low) large-scale mean momentum. The intermittency increases with the distance from the wall in the log layer, leading to the phase reversal. In the AM-dominating inner region, the strongest AM effect on small scales is aligned along the downstream edge of the large-scale low-momentum structures [32, 66]. However, in the opposite-effect-dominating outer region, the strongest opposite effect performs the preferential scale arrangement with fixed $\tau U_r/R$ between small scales and large scales. On the other hand, the value of the difference between the maximum and the minimum, i.e. the peak-to-peak value $V_{\rm pp}$ of the whole $\rho^{12}_{\rm AM}(\tau, y)$ map, is employed to measure the synthesised nonlinear effects. The results of $V_{\rm pp}$ versus Re_τ are presented in the top panel of figure 10. At fixed y_r, the $V_{\rm pp}$ value keeps stable in the present Re_τ range with relative scatters lower than 1.7%. This demonstrates again the Re_τ independence of $\rho^{12}_{\rm AM}(\tau, y)$. Averaged values of $V_{\rm pp}$ over the Re_τ range at 5 wall-normal locations are shown in the bottom panel. $V_{\rm pp}$ peaks at $y_r/R = 0.1$, because both AM and opposite effects are considerable there. At other 4 locations, although the minimum values of $\rho^{12}_{\rm AM}$ are comparable, as shown in the top panel of figure 11, the maximum values corresponding to the AM effect are smaller. The variation of $V_{\rm pp}$ with y_r reflects the severity of the phase reversal in the present wall-normal range.

To further compare the opposite effect (as well as the AM effect) by large scales at varied y_r, variations of $\rho^{12}_{\rm AM}$ with $\tau U_r/R$ at different pairs of y_r and y are presented

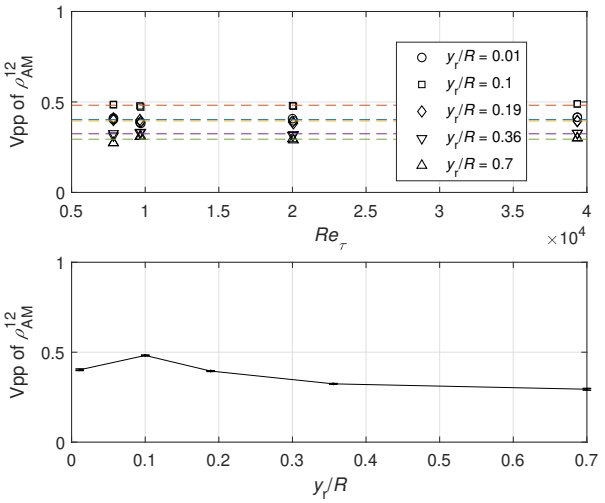

Figure 10: Top: $V_{\rm pp}$ versus Re_τ at $y_r/R = 0.01, 0.10, 0.19, 0.36, 0.70$ with $\circ$, $\square$, $\diamond$, $\triangledown$ and $\triangle$. Bottom: $V_{\rm pp}$ versus y_r/R.

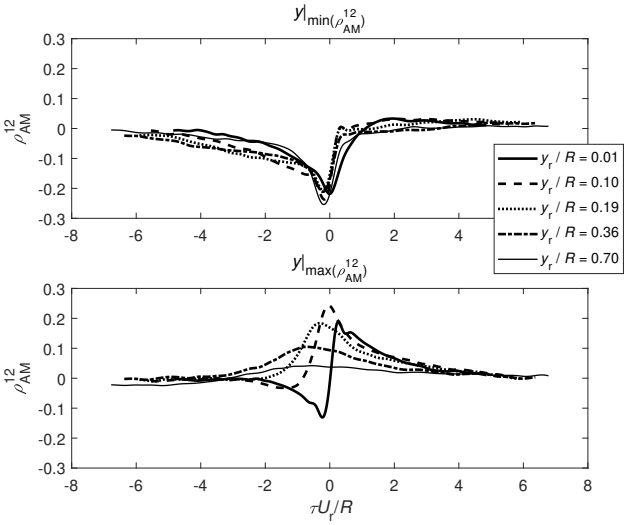

Figure 11: $\rho^{12}_{\rm AM}$ versus $\tau U_r/R$ at $y_r/R = 0.01, 0.10, 0.19, 0.36, 0.70$ (thick solid, dashed, dotted, dash-dotted and thin solid lines) with small-scale components at $y|_{\min(\rho^{12}_{\rm AM})}$ (top) and $y|_{\max(\rho^{12}_{\rm AM})}$ (bottom). $Re_\tau = 20000$.

in figure 11. In the top panel, curves are of small scales at $y|_{\min(\rho^{12}_{\rm AM})}$ with the strongest two-point opposite effect. In the bottom panel, curves are of small scales at $y|_{\max(\rho^{12}_{\rm AM})}$ with the strongest two-point AM effect. Different line-styles correspond to large scales at varied y_r/R. The friction Reynolds number is $Re_\tau = 20000$. For the strongest opposite effect, curves of $\rho^{12}_{\rm AM}(\tau)$ show a similar trend for different y_r. They decrease gradually from zero to the minimum, slightly upstream of the zero time-delay, then rapidly increase back to $\rho^{12}_{\rm AM} = 0$. This sim-

ilarity of the opposite effect is maintained even by the large scales at $y_r/R = 0.01$. The troughs are found at $\tau U_r/R = -0.195 \pm 0.019$ for $0.10 \leqslant y_r/R \leqslant 0.36$. This location is close to the results from R^{11}_{AM} (see in figure 7). It is argued that not only the time-delay of the minimum, but also the variation in a wide time-delay domain are maintained by the opposite effect. The reason should be that the large-scale mean momentum and the small-scale fluctuation amplitude in the intermittent non-turbulent zones and turbulent bulges follow a similar phase relation over the outer region.

For the strongest AM effect, curves at varied y_r differ greatly, although $y|_{\max(\rho^{12}_{AM})}$ is found to be fixed at $y/R = 0.01$. Large-scale components at $y_r/R = 0.01$ play a role in both the AM (see peak) and opposite (see trough) effects. The symmetry about $\tau = 0, \rho^{12}_{AM} = 0$ suggests the comparable contribution of large scales by means of two mechanisms: the AM effect on the downstream small scales, and the opposite effect on the upstream small scales. At $y_r/R = 0.10$, large scales mainly carry out the AM mechanism and maintain little opposite effect. In the outer region of $y_r/R \geqslant 0.19$, only the AM effect by large scales exists and it decays with increasing y_r. At $y_r/R = 0.70$, the AM effect decays to a very low level with $\rho^{12}_{AM} = 0.04$. Overall, the peak of $\rho^{12}_{AM}(\tau)$ moves upstream, reaches the maximum at $y_r/R = 0.10$ and vanishes as y_r increases. This evolution of the global strongest AM effect with y_r is not reflected by the one-point R^{11}_{AM} map in which the local strongest AM effect moves to downstream end with increasing y.

5. Conclusions

Taking advantages of the long pipe facility in CICLoPE, two sets of hot-wire measurements of the streamwise velocity with high-spatial resolution are performed, extending the friction Reynolds number Re_τ up to ~ 40000 for the hydraulically-smooth pipe flow. One measurement campaign is performed with a single-sensor probe scanning the pipe radius and the other with a fixed five-probe rake. Based on these data, one- and two-point correlation-based analyses are performed to investigate the coherent motions and the inter-scale interaction in the pipe flow. The high Re_τ facilitates the separation between different scales, while the high-spatial resolution guarantees unbiased estimates for coherent motions and inter-scale interactions. ODWT is utilised to reveal the scale dependence of correlated coherent motions, with the cut-off wavelengths of $\lambda_c/R = 1/2$ and 2π to separate LSMs and VLSMs.

The effects of Re_τ and the wall-bounded flow configuration are revealed by the present correlation-based analysis and by comparison with other lower-Re_τ studies on different flow configurations (e.g. BL, CH and pipe). Geometric features of full-scale velocity correlation maps maintain the Re_τ independence in the measured Re_τ range. The resulting inclination angle and integral length scale also show the Re_τ invariance, but a difference in the integral length scale is found between internal flows in pipe and CH and the external flow in BL. The correlation maps of the VLSMs show a certain degree of independence not only to Re_τ but also to the relative location in the inner region when normalised with outer scaling. The VLSMs keep the vertical coherence to the wall in the inner region, while for the LSMs, the local coherence gradually become less inclined as the reference point moves away from the wall. An upward shift of the one-point AM coefficient at zero time-delay $\rho^{11}_{AM}(\tau = 0)$ is observed for $y^+ > 30$ with increasing Re_τ. Since the outer intermittency in pipe flows is weaker than that in BLs [45], $\rho^{11}_{AM}(\tau = 0)$ in the wake region of pipe flows does not change as drastically as in the wake region of BLs. Although the two-point AM-function (R^{12}_{AM}) maps show increasing absolute intensity with Re_τ, the Re_τ invariance is observed in the two-point AM coefficient (ρ^{12}_{AM}) maps with the outer scaling in the extended Reynolds number range up to 40000. The resulting peak-peak value of the whole ρ^{12}_{AM} map is also independent of Re_τ, but depends on the large-scale reference locations.

Large-scale coherent structures modulate downstream small-scale fluctuations by the AM mechanism in the inner region, while negative correlated small-scale fluctuations are found upstream large-scale motions due to the opposite effect in the outer region, which is consistently observed in the one- and two-point AM analyses. Moreover, a new consistent finding about the strongest opposite effect is that the phase difference between large and small scales is independent with the outer-scaled wall-normal distance, which is different from the observation with the inner scaling by Baars et al. [32]. This implies that the outer opposite effect is governed by the outer length scale and the local mean velocity.

In addition to these consistent observations from one-point and two-point AM maps, other features drawn respectively from R^{11}_{AM} and ρ^{12}_{AM} are worth noting. One of the most significant features from the R^{11}_{AM} map is the well-fitted linear-log relation of the time shift with the outer-scaled wall-normal distance for the maximum and zero AM correlation and the maximum AM growth rate. The phase difference of the strongest AM effect maintains the log scaling as the profiles of mean velocity, wall-parallel turbulence intensities and even higher order moments [67]. Similarly, this might be interpreted from the perspective of inter-scale dynamics of self-similar attached eddy hierarchy [68]. Although these attached eddies grow from $y^+ \sim 80$, their ability of amplitude modulation can penetrate down to $y^+ < 10$. The AM-effect region is excluded by the wake region, which is consistent with the wall-attached VLSMs as shown in the wavelet spectra. For the opposite effect in the outer region, both one-point and two-point AM maps show a fixed phase of $\tau U_r/R \approx -0.2$. The opposite effect is proposed to be related to detached large-scale eddies which exist in the outer region (including the wake region). Although the self-similar attached/detached eddy model facilitates the understanding of linear-log behaviours by

the strongest AM and opposite effects, more direct verification is worthwhile. In particular, the structural difference between internal and external wall-bounded turbulence should be accounted to clarify the discrepancy in the phase behaviour by opposite effects in pipe flows and in BLs [32].

Another interesting point from the ρ^{12}_{AM} maps is that the zero net-modulation keeps an inclination angle of 4 degrees in the outer region. The zero net-modulation behaves differently in the log layer as shown by R^{11}_{AM} and in the whole outer region as shown by ρ^{12}_{AM}. The zero modulation implies that no net amplitude modulation exists, and it is neither subject to frequency modulation which is restricted in the near-wall region [32, 69]. The linear-log phase difference of the zero modulation in the log layer should be the nature of the superposition effect according to the predictive inner-outer model by Mathis et al. [28], while the inclination angle of about 4° in the whole outer region seems linked to the angle of the global-scale correlated motions.

Acknowledgements

This work was made possible by the financial support from the Joint-Cultivated Graduate Program of Chinese High-level University (Grant No. 201606250052), the European High Performance Infrastructures in Turbulence (Grant No. 312778), the National Natural Science Foundation of China (Grant No. 11872248) and the National Key Research and Development Plan of China (Grants No. 2017YFE0132000 and No. 2018YFB1501202).

References

[1] A. J. Smits, B. J. McKeon, I. Marusic, High-Reynolds number wall turbulence, Annu. Rev. Fluid Mech. 43 (2011) 353–375.

[2] I. Marusic, B. J. McKeon, P. A. Monkewitz, H. M. Nagib, A. J. Smits, K. R. Sreenivasan, Wall-bounded turbulent flows at high Reynolds numbers: Recent advances and key issues, Phys. Fluids 22 (2010) 065103.

[3] M. Samie, I. Marusic, N. Hutchins, M. K. Fu, Y. Fan, M. Hultmark, A. J. Smits, Fully resolved measurements of turbulent boundary layer flows up to $Re_\tau = 20,000$, J. Fluid Mech. 851 (2018) 391–415.

[4] R. J. Adrian, C. D. Meinhart, C. D. Tomkins, Vortex organization in the outer region of the turbulent boundary layer, J. Fluid Mech. 422 (2000) 1–54.

[5] N. Hutchins, I. Marusic, Evidence of very long meandering features in the logarithmic region of turbulent boundary layers, J. Fluid Mech. 579 (2007) 1–28.

[6] B. J. Balakumar, R. J. Adrian, Large- and very-large-scale motions in channel and boundary-layer flows, Philos. Trans. R. Soc. A 365 (2007) 665–681.

[7] N. Hutchins, K. Chauhan, I. Marusic, J. Monty, J. Klewicki, Towards reconciling the structure of boundary layers in the atmosphere and laboratory, Boundary Layer Meteorol. 145 (2012) 273–306.

[8] K. Chauhan, N. Hutchins, J. Monty, I. Marusic, Structure inclination angles in the convective atmospheric surface layer, Boundary Layer Meteorol. 147 (2013) 41–50.

[9] H. Liu, T. Bo, Y. Liang, The variation of large-scale structure inclination angles in high Reynolds number atmospheric surface layers, Phys. Fluids 29 (2017) 035104.

[10] M. Heisel, T. Dasari, Y. Liu, J. Hong, F. Coletti, M. Guala, The spatial structure of the logarithmic region in very-high-Reynolds-number rough wall turbulent boundary layers, J. Fluid Mech. 857 (2018) 704–747.

[11] K. T. Christensen, R. J. Adrian, Statistical evidence of hairpin vortex packets in wall turbulence, J. Fluid Mech. 431 (2001) 433–443.

[12] J. P. Monty, J. A. Stewart, R. C. Williams, M. S. Chong, Large-scale features in turbulent pipe and channel flows, J. Fluid Mech. 589 (2007) 147–156.

[13] C. E. Willert, J. Soria, M. Stanislas, J. Klinner, O. Amili, M. Eisfelder, C. Cuvier, G. Bellani, T. Fiorini, A. Talamelli, Near-wall statistics of a turbulent pipe flow at shear Reynolds numbers up to 40 000, J. Fluid Mech. 826 (2017) R5.

[14] J. Jiménez, Cascades in wall-bounded turbulence, Annu. Rev. Fluid Mech. 44 (2012) 27–45.

[15] J. Jiménez, Coherent structures in wall-bounded turbulence, J. Fluid Mech. 842 (2018) P1.

[16] D. Fiscaletti, R. de Kat, B. Ganapathisubramani, Spatial-spectral characteristics of momentum transport in a turbulent boundary layer, J. Fluid Mech. 836 (2018) 599–634.

[17] D. Fiscaletti, B. Ganapathisubramani, Characteristics of sources and sinks of momentum in a turbulent boundary layer, Phys. Rev. Fluids 3 (2018) 054601.

[18] J. H. Lee, H. J. Sung, Very-large-scale motions in a turbulent boundary layer, J. Fluid Mech. 673 (2011) 80–120.

[19] J. H. Lee, H. J. Sung, Comparison of very-large-scale motions of turbulent pipe and boundary layer simulations, Phys. Fluids 25 (2013) 045103.

[20] M. Guala, S. E. Hommema, R. J. Adrian, Large-scale and very-large-scale motions in turbulent pipe flow, J. Fluid Mech. 554 (2006) 521–542.

[21] S. C. C. Bailey, A. J. Smits, Experimental investigation of the structure of large- and very-large-scale motions in turbulent pipe flow, J. Fluid Mech. 651 (2010) 339–356.

[22] J. A. Sillero, J. Jiménez, R. D. Moser, Two-point statistics for turbulent boundary layers and channels at Reynolds numbers up to $\delta^+ \approx 2000$, Phys. Fluids 26 (2014) 105109.

[23] J. P. Monty, N. Hutchins, H. C. H. HG, I. Marusic, M. S. Chong, A comparison of turbulent pipe, channel and boundary layer flows, J. Fluid Mech. 632 (2009) 431–442.

[24] N. Hutchins, I. Marusic, Large-scale influences in near-wall turbulence, Phil. Trans. R. Soc. A 365 (2007) 647–664.

[25] P. R. Bandyopadhyay, A. K. M. F. Hussain, The coupling between scales in shear flows, Phys. Fluids 27 (1984) 2221.

[26] R. Mathis, N. Hutchins, I. Marusic, Large-scale amplitude modulation of the small-scale structures in turbulent boundary layers, J. Fluid Mech. 628 (2009) 311–337.

[27] I. Marusic, R. Mathis, N. Hutchins, Predictive model for wall-bounded turbulent flow, Science 329 (2010) 193–196.

[28] R. Mathis, N. Hutchins, I. Marusic, A predictive inner-outer model for streamwise turbulence statistics in wall-bounded flows, J. Fluid Mech. 681 (2011) 537–566.

[29] R. Mathis, I. Marusic, S. I. Chernyshenko, N. Hutchins, Estimating wall-shear-stress fluctuations given an outer region input, J. Fluid Mech. 715 (2013) 163–180.

[30] P. Schlatter, R. Örlü, Quantifying the interaction between large and small scales in wall-bounded turbulent flows: A note of caution, Phys. Fluids 22 (2010) 051704.

[31] S. Pirozzoli, M. Bernardini, Turbulence in supersonic boundary layers at moderate Reynolds number, J. Fluid Mech. 688 (2011) 120–168.

[32] W. J. Baars, K. M. Talluru, N. Hutchins, I. Marusic, Wavelet analysis of wall turbulence to study large-scale modulation of small scales, Exp. Fluids 56 (2015) 188.

[33] E. Dogan, R. Örlü, D. Gatti, R. Vinuesa, P. Schlatter, Quantification of amplitude modulation in wall-bounded turbulence, Fluid Dyn. Res. 51 (2019) 011408.

[34] J. C. R. Hunt, J. F. Morrison, Eddy structure in turbulent boundary layers, Eur. J. Mech. B 19 (2000) 673–694.

[35] M. Guala, M. Metzger, B. J. McKeon, Interactions within the

turbulent boundary layer at high Reynolds number, J. Fluid Mech. 666 (2011) 573–604.
[36] W. J. Baars, N. Hutchins, I. Marusic, Reynolds number trend of hierarchies and scale interactions in turbulent boundary layers, Phil. Trans. R. Soc. A 375 (2017) 20160077.
[37] L. Agostini, M. Leschziner, The connection between the spectrum of turbulent scales and the skin-friction statistics in channel flow at $Re_\tau = 4200$, J. Fluid Mech. 871 (2019) 22–51.
[38] S. Chernyshenko, Extension of QSQH theory of scale interaction in near-wall turbulence to all velocity components, J. Fluid Mech. 916 (2021) A52.
[39] G. Iacobello, L. Ridolfi, S. Scarsoglio, A review on turbulent and vortical flow analyses via complex networks, Physica A 563 (2021) 125476.
[40] R. Örlü, P. H. Alfredsson, On spatial resolution issues related to time-averaged quantities using hot-wire anemometry, Exp. Fluids 49 (2010) 101–110.
[41] A. Talamelli, F. Persiani, J. H. M. Fransson, P. H. Alfredsson, A. V. Johansson, H. M. Nagib, J. D. Rüedi, K. R. Sreenivasan, P. A. Monkewitz, CICLoPE - a response to the need for high Reynolds number experiments, Fluid Dyn. Res. 41 (2009) 021407.
[42] G. Bellani, A. Talamelli, The Final Design of the Long Pipe in CICLOPE, in: J. Peinke, G. Kampers, M. Oberlack, M. Waclawczyk, A. Talamelli (Eds.), Progress in Turbulence, Vol. 165 of VI, Springer, 2016, pp. 205–209.
[43] R. Örlü, T. Fiorini, A. Segalini, G. Bellani, A. Talamelli, P. H. Alfredsson, Reynolds stress scaling in pipe flow turbulence — first results from CICLoPE, Phil. Trans. Roy. Soc. A 375 (2089) (2017) 20160187.
[44] S. Discetti, G. Bellani, R. Örlü, J. Serpieri, C. Sanmiguel Vila, M. Raiola, X. Zheng, L. Mascotelli, A. Talamelli, A. Ianiro, Characterization of very-large-scale motions in high-Re pipe flows, Exp. Therm. Fluid Sci. 104 (2019) 1–8.
[45] S. Zimmerman, J. Philip, J. Monty, A. Talamelli, I. Marusic, B. Ganapathisubramani, R. J. Hearst, G. Bellani, R. Baidya, M. Samie, X. Zheng, E. Dogan, L. Mascotelli, J. Klewicki, A comparative study of the velocity and vorticity structure in pipes and boundary layers at large Reynolds numbers, J. Fluid Mech. 869 (2019) 182–213.
[46] R. Baidya, W. J. Baars, S. Zimmerman, M. Samie, R. J. Hearst, E. Dogan, L. Mascotelli, X. Zheng, G. Bellani, A. Talamelli, B. Ganapathisubramani, N. Hutchins, I. Marusic, J. Klewicki, J. Monty, Simultaneous skin friction and velocity measurements in high Reynolds number pipe and boundary layer flows, J. Fluid Mech. 871 (2019) 377–400.
[47] R. Mathis, J. P. Monty, N. Hutchins, I. Marusic, Comparison of large-scale amplitude modulation in turbulent boundary layers, pipes, and channel flows, Phys. Fluids 21 (2009) 111703.
[48] Center for International Collaboration on Long Pipe Experiments, `http://www.ciclope.unibo.it` (2013).
[49] Y. Fan, G. Arwatz, T. W. V. Buren, D. E. Hoffman, M. Hultmark, Nanoscale sensing devices for turbulence measurements, Exp. Fluids 56 (2015) 138.
[50] T. Fiorini, Turbulent pipe flow - high resolution measurements in CICLoPE, Ph.D. thesis, Dipartimento Ingegneria Industriale, Università di Bologna, Forlì, Italy (2017).
[51] R. Örlü, R. Vinuesa, Thermal anemometry, in: Experimental Aerodynamics (Eds. Discetti and Ianiro), CRC Press, 2017, pp. 257–304.
[52] K. M. Talluru, V. Kulandaivelu, N. Hutchins, I. Marusic, A calibration technique to correct sensor drift issues in hot-wire anemometry, Meas. Sci. Technol. 25 (2014) 105304.
[53] N. Hutchins, T. B. Nickels, I. Marusic, M. S. Chong, Hot-wire spatial resolution issues in wall-bounded turbulence, J. Fluid Mech. 635 (2009) 103–136.
[54] A. J. Smits, J. P. Monty, M. Hultmark, S. C. C. Bailey, N. Hutchins, I. Marusic, Spatial resolution correction for wall-bounded turbulence measurements, J. Fluid Mech. 676 (2011) 41–53.
[55] J. C. del Álamo, J. Jiménez, P. Zandonade, R. D. Moser, Scaling of the energy spectra of turbulent channels, J. Fluid Mech. 500 (2004) 135–144.
[56] I. Marusic, W. Heuer, Reynolds number invariance of the structure inclination angle in wall turbulence, Phys. Rev. Lett. 99 (2007) 114504.
[57] J. P. Monty, Developments in smooth wall turbulent duct flows, Ph.D. thesis, Department of Mechanical and Manufacturing Engineering, the University of Melbourne, Melbourne, Australia (2005).
[58] M. Farge, Wavelet transforms and their applications to turbulence, Ann. Rev. Fluid Mech. 24 (1992) 395–457.
[59] S. G. Mallat, A theory for multiresolution signal decomposition: the wavelet representation, IEEE Trans. PAMI 11 (7) (1989) 674–693.
[60] S. W. Smith, Introduction to Digital Filters, in: Digital Signal Processing, A Practical Guide for Engineers and Scientists, Elsevier Inc., 2003, pp. 261–276.
[61] X. Zheng, N. Jiang, Experimental study on spectrum and multiscale nature of wall pressure and velocity in turbulent boundary layer, Chin. Phys. B 24 (6) (2015) 064702.
[62] R. Mathis, I. Marusic, N. Hutchins, K. R. Sreenivasan, The relationship between the velocity skewness and the amplitude modulation of the small scale by the large scale in turbulent boundary layers, Phys. Fluids 23 (2011) 121702.
[63] K. M. Talluru, R. Baidya, N. Hutchins, I. Marusic, Amplitude modulation of all three velocity components in turbulent boundary layers, J. Fluid Mech. 746 (2014) R1.
[64] D. Chung, B. J. McKeon, Large-eddy simulation of large-scale structures in long channel flow, J. Fluid Mech. 661 (2010) 341–364.
[65] N. Hutchins, Large-scale structures in high Reynolds number wall-bounded turbulence, in: A. Talamelli, M. Oberlack, J. Peinke (Eds.), Progress in turbulence V, Vol. 149, Springer International Publishing, 2014, p. 75–83.
[66] N. Hutchins, J. P. Monty, B. Ganapathisubramani, H. C. H. Ng, I. Marusic, Three-dimensional conditional structure of a high-Reynolds-number turbulent boundary layer, J. Fluid Mech. 673 (2011) 255–285.
[67] C. Meneveau, I. Marusic, Generalized logarithmic law for high-order moments in turbulent boundary layers, J. Fluid Mech. 719 (2013) R1.
[68] I. Marusic, J. P. Monty, Attached eddy model of wall turbulence, Annu. Rev. Fluid Mech. 51 (2019) 49–74.
[69] B. Ganapathisubramani, N. Hutchins, J. P. Monty, D. Chung, I. Marusic, Amplitude and frequency modulation in wall turbulence, J. Fluid Mech. 712 (2012) 61–91.